

Quantum photonic integrated circuits based on tunable dots and tunable cavities

M. Petruzzella, S. Birindelli, F. M. Pagliano, D. Pellegrino, Ž. Zobenica, L. H. Li, E. H. Linfield, and A. Fiore

Citation: *APL Photonics* **3**, 106103 (2018); doi: 10.1063/1.5039961

View online: <https://doi.org/10.1063/1.5039961>

View Table of Contents: <http://aip.scitation.org/toc/app/3/10>

Published by the [American Institute of Physics](#)

Articles you may be interested in

[Photon pair generation using a silicon photonic hybrid laser](#)

APL Photonics **3**, 106104 (2018); 10.1063/1.5040118

[Perspective: The future of quantum dot photonic integrated circuits](#)

APL Photonics **3**, 030901 (2018); 10.1063/1.5021345

[Tutorial: Integrated-photonic switching structures](#)

APL Photonics **3**, 021101 (2018); 10.1063/1.5017968

[Germanium microlasers on metallic pedestals](#)

APL Photonics **3**, 106102 (2018); 10.1063/1.5025705

[Invited Article: Tuning and stabilization of optomechanical crystal cavities through NEMS integration](#)

APL Photonics **3**, 100801 (2018); 10.1063/1.5042225

[Design, fabrication, and metrology of \$10 \times 100\$ multi-planar integrated photonic routing manifolds for neural networks](#)

APL Photonics **3**, 106101 (2018); 10.1063/1.5039641

AIP | Conference Proceedings

Get **30% off** all
print proceedings!

Enter Promotion Code **PDF30** at checkout



Quantum photonic integrated circuits based on tunable dots and tunable cavities

M. Petruzzella,^{1,a} S. Birindelli,¹ F. M. Pagliano,¹ D. Pellegrino,¹ Ž. Zobenica,¹ L. H. Li,² E. H. Linfield,² and A. Fiore¹

¹*Department of Applied Physics and Institute for Photonic Integration, Eindhoven University of Technology, 5612 AZ Eindhoven, The Netherlands*

²*School of Electronic and Electrical Engineering, University of Leeds, Leeds LS2 9JT, United Kingdom*

(Received 13 May 2018; accepted 17 July 2018; published online 16 August 2018)

Quantum photonic integrated circuits hold great potential as a novel class of semiconductor technologies that exploit the evolution of a quantum state of light to manipulate information. Quantum dots encapsulated in photonic crystal structures are promising single-photon sources that can be integrated within these circuits. However, the unavoidable energy mismatch between distant cavities and dots, along with the difficulties in coupling to a waveguide network, has hampered the implementation of circuits manipulating single photons simultaneously generated by remote sources. Here we present a waveguide architecture that combines electromechanical actuation and Stark-tuning to reconfigure the state of distinct cavity-emitter nodes on a chip. The Purcell-enhancement from an electrically controlled exciton coupled to a ridge waveguide is reported. Besides, using this platform, we implement an integrated Hanbury-Twiss and Brown experiment with a source and a splitter on the same chip. These results open new avenues to scale the number of indistinguishable single photons produced on-demand by distinct emitters. © 2018 Author(s). All article content, except where otherwise noted, is licensed under a Creative Commons Attribution (CC BY) license (<http://creativecommons.org/licenses/by/4.0/>). <https://doi.org/10.1063/1.5039961>

I. INTRODUCTION

The ability to program the properties of deterministic single-photon sources such as quantum dots (QDs) and their electromagnetic environment will play a crucial role in the realization of large-scale quantum photonic integrated circuits (QPICs) able to simulate complex molecules and to perform boson sampling experiments.^{1,2} These emitters are typically embedded in nano-cavities, such as photonic crystal (PhC) defects, either to enhance the generation rate and the coherence properties of their emission via the Purcell effect or to access nonlinearities present in the strong-coupling regime.³ Despite the impressive progress with the realization of bright and indistinguishable emission from single excitons coupled to semiconductor cavities,⁴ which have led to the first commercially available deterministic single-photon sources,^{5,6} a number of open challenges exist for the implementation of circuits operating with many parallel QD sources. One of the main difficulties arises from the lack of control on the nanoscale properties of as-grown QDs, along with the fabrication disorder which also affects the optical characteristics of nanocavities. These effects induce an unpredictable shift in the energy of both emitters and cavity resonances which must be corrected via post-fabrication methods. Recently, several schemes have been implemented to control the cavity spectrum, namely, thermal methods,⁷ photochromic materials,⁸ photo-oxidation,⁹ free carrier injection,^{10,11} and nano-electromechanical systems,^{12–15} while a number of techniques based on electric, magnetic, and strain control have been successfully employed to tune the QD exciton's energy.³ In this regard, a key requirement for scaling the number of energy-indistinguishable sources for both intra- and inter-chip

^aElectronic mail: m.petruzzella@tue.nl

applications consists in simultaneously reconfiguring the status of multiple cavity quantum electrodynamics (c-QED) nodes by external controls.

An additional open problem for future QPICs is represented by the integration of these tunable nodes with a waveguide (WG) architecture. The transfer of the quantum state to standard ridge waveguides (RWs) offers the possibility to exploit pre-existing optical components developed for classical photonic circuits in the context of QPICs, such as phase shifters, filters, and couplers. Besides, RWs can be employed not only to transport single photons to other elements of the chip with low loss but also to distribute the optical pump among many sources, in order to simultaneously trigger the single-photon emission from remote cavity-emitter nodes. The coupling of Purcell-enhanced single photons generated in a photonic crystal cavity (PhCC) to a ridge waveguide has been previously demonstrated, either employing a monolithic approach relying on a single material¹⁶ or, more recently, adopting a hybrid GaAs/SiN photonic crystal nanobeam.¹⁷ However, the deterministic control of the dot and cavity wavelength, essential for multi-source experiments, and the integration with other photonic elements were not addressed in these demonstrations.

In this paper, we describe the integration of multiple tunable QD sources within a photonic circuit. The nano-mechanical reconfiguration of a double-membrane PhC cavity is employed to electrically control the frequency of a cavity mode coupled to a ridge waveguide. Furthermore, by regulating the Stark field across the dots embedded in these devices, a Purcell-enhanced excitonic emission is transferred to a waveguide network. In order to prove the flexibility of this approach, we have also realized a beam splitter compatible with this platform. A Hanbury-Twiss and Brown experiment (HBT) with a source and a splitter fabricated on the same chip is presented. Finally, we discuss the integration of multiple c-QED nodes on the same photonic circuit. The developed WG-coupled architecture equipped with electrical gates has been adopted to suppress the energy mismatch among separate cavities and emitters.

II. PLATFORM DESCRIPTION

The main core of our photonic platform consists of two suspended PhC membranes that are optically coupled along the growth direction, Fig. 1(a). By controlling the reverse bias V_{CAV} of a p-i-n diode fabricated across these membranes, the symmetric (S) and anti-symmetric (AS) supermodes of the structure can be shifted in energy via capacitive actuation.¹⁴ Besides, by growing self-assembled dots within the intrinsic region of a second p-i-n junction incorporated into the top membrane, the energy of the QD excitonic lines can be independently controlled via the application of a voltage V_{QD} through the quantum-confined Stark effect.¹⁸ In what follows, these two diodes are referred to as QD diode and cavity diode, respectively. For the fabrication details, we refer to Sec. II of the [supplementary material](#).

Here the sample layer stack consists of a pair of 170 nm thick GaAs membranes, separated by a 240 nm thick $Al_{0.7}Ga_{0.3}As$ inter-layer. A layer of self-assembled InAs quantum dots emitting around 1300 nm at 4 K is grown in the middle of the top membrane.¹⁹ Besides, a bottom 1.5 μm -thick sacrificial layer decouples the pair of membranes from the GaAs substrate. The bottom 50 nm-thick part of the top slab is n-doped, while the upper 50 nm thick region of both membranes is p-doped ($p_{QD} = 1.5 \times 10^{18} \text{ cm}^{-3}$, $n = p_{CAV} = 2 \times 10^{18} \text{ cm}^{-3}$). A crucial point in the fabrication process consists in the selective removal of the AlGaAs layers. Specifically, we adopt an anisotropic etching which stops at specific crystallographic planes of the sacrificial layer. In this way, both suspended and supported structures can be realized during the same lithographic step by controlling their critical width, similar to what was previously realized for single-membrane PhCs.¹⁶ By using a HCl solution at 1 °C, a ridge waveguide can be fabricated, as shown in Fig. 1(d). This element is mechanically supported by a pair of inverted trapezoidal pedestals located underneath the bottom GaAs membrane and in between the two membranes. When the waveguide is aligned to the (011) crystallographic direction, the angle of this $Al_{0.7}Ga_{0.3}As$ trapezoidal support is $\approx 52^\circ$. The ridge waveguides realized using this method are characterized by a relatively low loss coefficient $\bar{\alpha} = 1.9 \pm 0.3 \text{ cm}^{-1}$ (see S3 of the [supplementary material](#)). Importantly, the possibility to pattern mechanically movable elements together with a standard photonic circuitry simplifies the process flow and avoids misalignment errors in multiple lithographic steps.

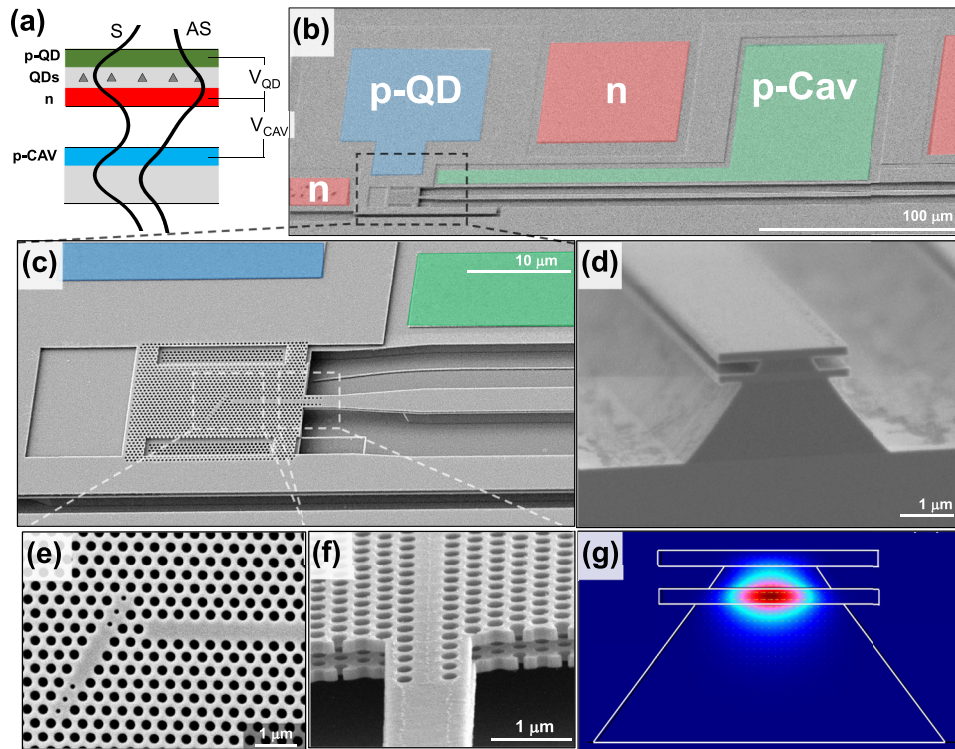


FIG. 1. (a) Sketch of the double-membrane device. [(b)–(g)] SEM pictures of a waveguide-coupled mechanically tunable cavity. (b) Top view of the full device, including the mesas of the two diodes. (c) Transition from the suspended PhC region to the supported ridge waveguide. (d) Cross section of the ridge waveguide. (e) Zoom-in in the cavity region. (f) Tilted view of suspended membranes. (g) FEM simulation of the fundamental TE mode of the ridge waveguide.

The scheme employed to couple a localized photonic crystal cavity (PhCC) mode to a supported ridge waveguide makes use of two consecutive transitions realized adopting this fabrication method [Figs. 1(c), 1(e), and 1(f)]. First (A) the suspended cavity is coupled to the broadband propagating mode of a suspended photonic crystal waveguide (PhCWG), created by omitting a row from the PhC lattice. Then (B), a mode adapter is employed to optically and mechanically interconnect this region to a ridge waveguide that is mechanically supported by using an AlGaAs pedestal. These two transitions are separately discussed in the next paragraphs.

A. PhCC-PhCWG coupling

The geometrical configurations to evanescently couple a single-membrane PhCC mode and a propagating PhCWG mode have been previously investigated.^{16,20–30} High coupling efficiencies can be obtained by maximizing the spatial and the frequency overlap between the propagating modes supported by the waveguide and the modes localized in the cavity.²⁰

In this work, we employ a double-membrane modified L3 cavity which consists of three in-line holes omitted from a hexagonal periodic lattice. The radii and positions of 10 holes surrounding the cavity defect have been optimized in order to obtain narrow PhC resonances featuring a large (≈ 20 nm) free spectral range.³¹ Similar to the single-membrane case,²⁶ the in-plane spatial profile of these modes extends in a direction tilted with respect to the cavity axis. This suggests that in-line coupling is not optimal. Here we chose to tilt the PhCWG to 60° with respect to the cavity axis,²⁶ as shown in Fig. 1(e). In addition, in order to match the frequency of the lower order modes of the modified L3 cavity with the dispersion of the fundamental Bloch mode of the PhCWG, the width of the PhCWG is set to $w = 1.1a\sqrt{3}$, where a is the lattice constant of the crystal.

With the aim of estimating the coupling efficiencies of the PhCC-PhCWG transition, we study the quality factors (Qs) of the AS modes in the presence of the waveguide channel. Similar considerations

are valid for the S modes. The waveguide introduces a decay channel in the unperturbed cavity mode. Given the simulated quality factor of the isolated cavity Q_0 , the loaded quality factor in the presence of the waveguide Q_{loaded} is given by³²

$$\frac{1}{Q_{loaded}} = \frac{1}{Q_0} + \frac{1}{Q_{wg}}, \quad (1)$$

where $1/Q_{wg}$ is proportional to the loss rate into the waveguide. The loaded Q-factor computed by 3D finite element method (FEM) simulations for the AS fundamental Y1 and first-order Y2 mode of the PhC cavity is plotted in Fig. 2(a) as a function of the number holes nH composing the PhCC-PhCWG barrier. The E_y component of these modes in middle of the top membrane is reported in Fig. 2(a) (inset). Q_{loaded} of both modes tends to the value of the unloaded Q-factor for $nH = 4$. While a monotonic increase of the Q-factor is experienced by Y1 when the barrier length is increased, a local minimum is observed for $nH = 3$ for the mode Y2. This behavior can be attributed to the spatial oscillations of the evanescent tail of the PhC modes.^{26,27} By increasing the barrier length from 1 to 5 holes, Q_{wg} can be varied from 2.7×10^2 to 6.8×10^6 for the Y1 mode and from 1.4×10^3 to 1.2×10^6 for the Y2 mode. The efficiency for coupling photons from the cavity to the waveguide, $\eta_c = Q_{loaded}/Q_{wg}$, where Q_{wg} is calculated from Eq. (1), is reported in Fig. 2(b). A trade-off between transmission efficiency and quality factor arises from these simulations. Depending on the specific

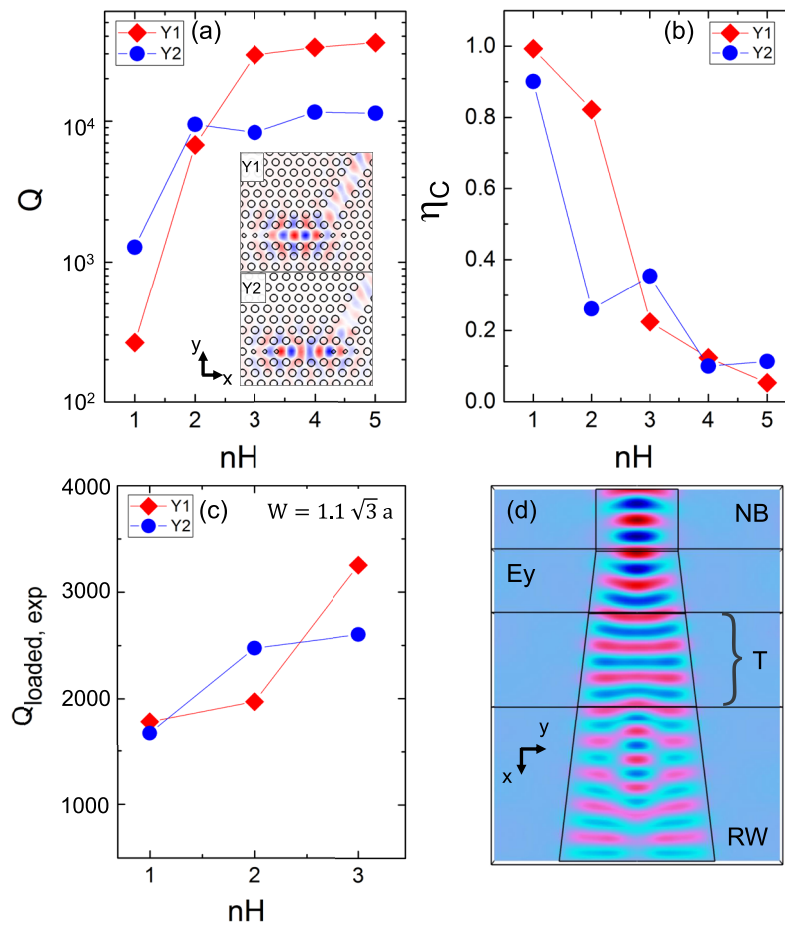


FIG. 2. 3D-FEM simulated Q-factors (a) and transmission coefficient (b) of the antisymmetric fundamental (Y1) and first-order (Y2) cavity modes diagonally coupled to a PhCWG. (Inset) E_y component of the cavity eigenmodes for a barrier length $nH = 1$. (c) Experimental Q-factors. (d) Calculated electric field of the AS mode along the taper, from the free-standing nanobeams (NB) to the ridge waveguides (RW) via the transition region T, where the bottom AlGaAs layer is etched while the inter-membrane AlGaAs layer is preserved.

application, high efficiency can be preferred to high Q factors, unless the strong-coupling regime is needed.

In order to validate these predictions, we fabricated devices comprising $nH = 1, 2$, and 3 with a varying PhCWG width W with lattice constant $a = 380$ nm and a radius $r = 0.31a$. Figure 2(c) shows the experimental quality factors extracted from the micro-photoluminescence (PL) spectra of the cavity modes as a function of the number of holes of the barrier for the two AS modes Y1 (red diamonds) and Y2 (blue dots). We focus on AS modes since the S modes are not evident in the PL spectra due to the membrane thickness asymmetry induced by the non-selectivity of the etching process.³³ Here the width of PhCWG is set to $W = 1.1\sqrt{3}a$, while the Q-factors for different waveguide widths are reported in S4 of the [supplementary material](#). An increase of the experimental $Q_{loaded,exp}$ as a function of the barrier length is observed, indicating a reduced coupling efficiency. The experimental quality factors of the uncoupled AS Y1 and Y2 mode, measured over 5 different devices produced in the same fabrication run, are $Q_0(Y1) = 3400 \pm 200$ and $Q_0(Y2) = 3300 \pm 300$. These values are identified with the loss channels associated with fabrication disorder in this process. Since the presence of the waveguide does not substantially alter the field profile of the cavity mode, we assume that WG-coupled cavities are affected by the same disorder-induced loss channel. We exclude that the reduction of the quality factors with respect to the simulated values arises from absorption due to the doping layers since quality factors above 15 000 have been experimentally demonstrated on double-membrane devices having a similar epitaxial structure.³¹

In Table I, we report the experimental coupling efficiency derived following Ref. 26 and Eq. (1).

From this analysis, we conclude that the designs $nH = 1, 2$ provide a good transmission into the waveguide for both modes, while preserving a quality factor high enough for obtaining a sizeable Purcell enhancement. These features are essential for filtering a single dot line among the multiple excitonic transitions produced with non-resonant excitation and to mitigate effects originated by charge noise if resonant excitation strategies are used.⁴ While a quantitative comparison between the experimental and the theoretical coupling efficiencies is hampered by the presence of disorder, it is worth mentioning that increasing the barrier length to $nH = 3$ results in the collection of only one mode (Y2) from the WG. This is due to the different in-plane spatial confinement of the PhCC modes, as predicted by FEM simulations [see Fig. 2(b)]. This aspect is particularly appealing for applications in classical integrated photonics that require a large free spectral range combined with a narrow resonance ($Q(Y2) \approx 2600$), such as integrated spectrometers³¹ and optical switches.³⁴

B. Mode adapter

In this section, we discuss the design of a tapered bridge, engineered to transfer the PhC modes created in the suspended membranes to the trapezoidal ridge waveguides. The output of the photonic crystal section is connected to two suspended nanobeams (NBs), which supports a pair of TE modes, having a symmetric and anti-symmetric field profile and a calculated effective refractive index $n_{NB,S} = 2.623$ and $n_{NB,AS} = 2.564$, respectively. An abrupt transition between this region and the ridge waveguide would induce high losses arising from their index mismatch $\Delta n_{eff} > 0.54$. A convenient solution to overcome this problem consists in employing an adiabatic taper to convert the modes of the double nanobeams into the RW. The width of the nanobeams can be progressively increased along the propagation direction in order to gradually create an AlGaAs spacer both in between the two membranes and underneath the bottom membrane. The width of the basis of this AlGaAs trapezoidal

TABLE I. PhCC-PhCWG coupling coefficients.

nH	$\eta_c(Y1)$	$Q(Y1)$	$\eta_c(Y2)$	$Q(Y2)$
1	0.48 ± 0.08	1785	0.51 ± 0.1	1677
2	0.42 ± 0.04	1973	0.27 ± 0.09	2475
3	0.04 ± 0.01	3254	0.23 ± 0.06	2602

pedestal increases according to the width of the taper. After a critical width of $w_{cr} \approx 1.65 \mu\text{m}$, a supporting post is produced sustaining both membranes, see Fig. 1(c).

We design a linear taper characterized by a length of $L_{\text{tap}} = 8 \mu\text{m}$ and an in-plane angle of $\theta = 6.7^\circ$. If the tapering angle is sufficiently small, the initial mode can be adiabatically converted into the fundamental mode of the output waveguide.³⁵ In principle, the longer the taper, the lower the losses associated to this transition. However, in the case of the dual-layer architecture, the taper cannot be arbitrary long, due to the presence of buckling,³⁶ as observed for structures longer than $10 \mu\text{m}$.

In the remaining part of the text, we focus on the AS mode. The transmission of the mode adapter is simulated using 3D-FEM algorithms. The E_y component of the propagating AS mode is shown in Fig. 2(d), while the simulation methods and the results for the S mode are discussed in the [supplementary material](#). At the transition point, where the AlGaAs pedestals are formed, light scattering is manifested for both modes and part of incoming light is coupled to the underlying substrate. The calculated transmission coefficient for the S and AS mode is $\eta_{t,S} = 40.5\%$ and $\eta_{t,AS} = 29.6\%$, respectively. A better coupling might be obtained by increasing the length of the suspended part of the taper by making use of lateral supporting tethers without introducing detrimental losses.³⁷ For example, by engineering the separation and the width of the lateral tethers a loss around 0.2 dB per tether has been demonstrated in a single-membrane platform.³⁸ These concepts can be implemented in the future in the GaAs double-membrane platform.

III. TUNING RESULTS

In what follows we present the low-temperature (10 K) tuning capabilities of the waveguide-coupled c-QED nodes described in Sec. II. The cavity and dot diodes are fabricated in a lateral configuration parallel to the waveguide, as shown in Fig. 1(b). Additionally, a series of $2 \mu\text{m}$ wide trenches are deeply etched around the contact regions to electrically isolate the two diodes.

We first investigate the electromechanical actuation of a WG-coupled PhCC, characterized by $nH = 3$. Figure 3 shows the cavity emission collected from a lensed fiber located at the RW facet, 1 mm away from the PhC region. Here the cavity region is excited with a 780 nm continuous-wave (CW) laser spot with relatively high power ($P = 0.8 \text{ mW}$) while the cavity voltage V_{CAV} is varied from 0 V to -3 V .

The in-plane symmetry of the cavity mode is identified with the mode Y2, while its vertical symmetry is recognized as anti-symmetric from the tuning direction. A maximum blue shift of 3.25 nm is obtained for this device. Here the tuning range is limited by the residual buckling produced during the fabrication process and can be increased by implementing stress-releasing designs.³⁶ Nevertheless, it is sufficient to correct for most of the experimental deviations among resonant frequencies of nominally identical cavities in our fabrication process. The tuning rate increases as a function of the cavity voltage, as expected by the non-linear behavior of the actuation which also produces pull-in when the cavity voltage is decreased below $V_{\text{CAV}} \approx -5 \text{ V}$.¹⁴

Next, we tune the energy of an exciton located in a PhCC and collect its emission from the RW facet. Figure 4(a) shows the low-temperature side-PL map collected by exciting the cavity region of a device having a barrier length $nH = 2$. As a reference, the top panel shows the PL spectrum of the cavity mode under investigation acquired with high excitation power ($P = 0.7 \text{ mW}$). This is characterized by a quality factor $Q \approx 1800$ and has been identified with the mode Y1_{AS}. The bottom panel shows the single-exciton PL signal collected at lower power ($P = 10 \mu\text{W}$) when the QD voltage is swept from 300 mV to 420 mV in the forward bias. A clear enhancement of all the QD lines—and in particular of QD1 indicated by an arrow—is evident when they cross the cavity mode central wavelength, indicative of the acceleration of their spontaneous emission via the Purcell effect.

We performed time-resolved photoluminescence (TR-PL) experiments employing a 780 nm pulsed laser operating at a repetition rate $f = 80 \text{ MHz}$ in order to investigate the dynamics of the exciton line QD1 for different values of the cavity-emitter detuning, see Fig. 4(b). When the dot line is positioned on resonance with the cavity mode (red dots, $V_{\text{QD}} = 360 \text{ mV}$, $\lambda_1 = 1278.42 \text{ nm}$), a clear reduction of its decay time is visible compared to the case when it is blue-tuned (black dots,

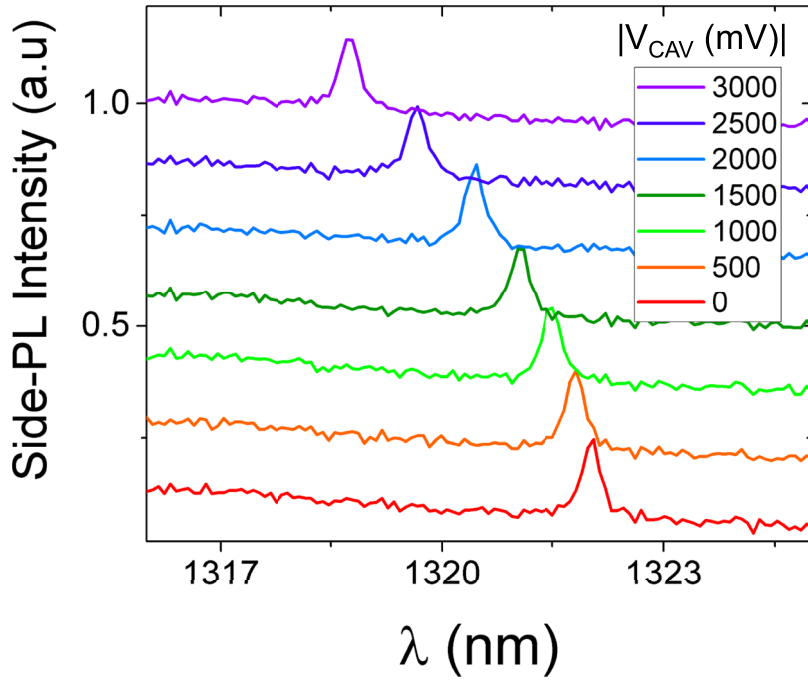


FIG. 3. Low-temperature ($T = 10$ K) electromechanical tuning of the antisymmetric $Y2$ mode of a WG-coupled double-membrane PhC cavity. The emission is collected from the side facet of the ridge waveguide and the cavity is excited with a power $P = 0.8$ mW.

$V_{\text{QD}} = 420$ mV, $\lambda_2 = 1277.42$ nm) or red-tuned (blue dots, $V_{\text{QD}} = 310$ mV, $\lambda_3 = 1279.34$ nm) with respect to the central wavelength of the cavity mode λ_{CAV} . The emission from the QD ensemble outside the PhC region (bulk) of the same sample is reported for reference (green dots). Both the on-resonance and the off-resonance decays are well represented by a double exponential decay (continuous lines), where the slower decay (> 2 ns) is associated with the presence of the dark exciton transition.³⁹ In general, the fast decay rate of an exciton in a PhC-diode is given by three contributions: $\tau^{-1} = \tau_{\text{PhC}}^{-1} + \tau_{\text{Leaky}}^{-1} + \tau_{\text{tun}}^{-1}$, where τ_{PhC}^{-1} is associated with the decay rate into the cavity mode, τ_{tun}^{-1} is related to the tunneling rate out of the dot, and τ_{Leaky}^{-1} is the decay rate into the leaky modes, which is typically negligible.⁴⁰ From the exponential fit of the decay curves, we obtain $\tau_1 = (340 \pm 20)$ ps for the fast decay measured for the resonance condition, $\tau_2 = (710 \pm 30)$ ps and $\tau_3 = (650 \pm 30)$ ps for the blue- and red-shifted configurations, respectively. Although the absolute detuning from the cavity wavelength is slightly larger for λ_3 , we observe that $\tau_3 < \tau_2$. This constitutes an indication that tunneling effects are not negligible in this range of Stark-voltage values. We indeed measured a linear dependence of the tunneling rate on V_{QD} for dots embedded in a region located outside the PhC in another sample, for the narrow range of the Stark-voltage values investigated in these experiments.⁴¹ Since the tunneling rate was also observed to depend on the specific excitation condition, the values measured outside of the cavity cannot be directly used to estimate the tunneling rate for this experiment. Instead, by assuming a linear dependence of τ_{tun}^{-1} on the applied voltage and that

$$\frac{\tau_{\text{PhC}}(\lambda_i)}{\tau_{\text{PhC}}(\lambda_{\text{CAV}})} = 1 + 4Q^2 \left(\frac{\lambda_i}{\lambda_{\text{CAV}}} - 1 \right)^2 \quad (2)$$

for $i = 1, 2, 3$,⁴² we derived $\tau_{\text{PhC}}(\lambda_1) \approx 600$ ps and $\tau_{\text{tun}}(\lambda_1) \approx 790$ ps at resonance. A Purcell factor of $F_p = \frac{\tau_{\text{bulk}}}{\tau_{\text{PhC}}} \approx 2.4$ is thus calculated from the extracted decay time in the cavity mode and the decay time $\tau_{\text{bulk}} \approx 1430$ ps measured from dots located in a bulk region in a bias condition such that tunneling is negligible. This value is lower than the theoretical Purcell enhancement $F_p = 3/4\pi(\lambda/n)^3 Q/V = 216$, [where $V = 1.95(\lambda/n)^3$ has been calculated by FEM simulation], presumably due to the spatial misalignment between the maximum of the cavity field and the position of the emitter. Finally, the efficiency of the dot emission into the cavity mode, in the presence of the nonradiative decay channel

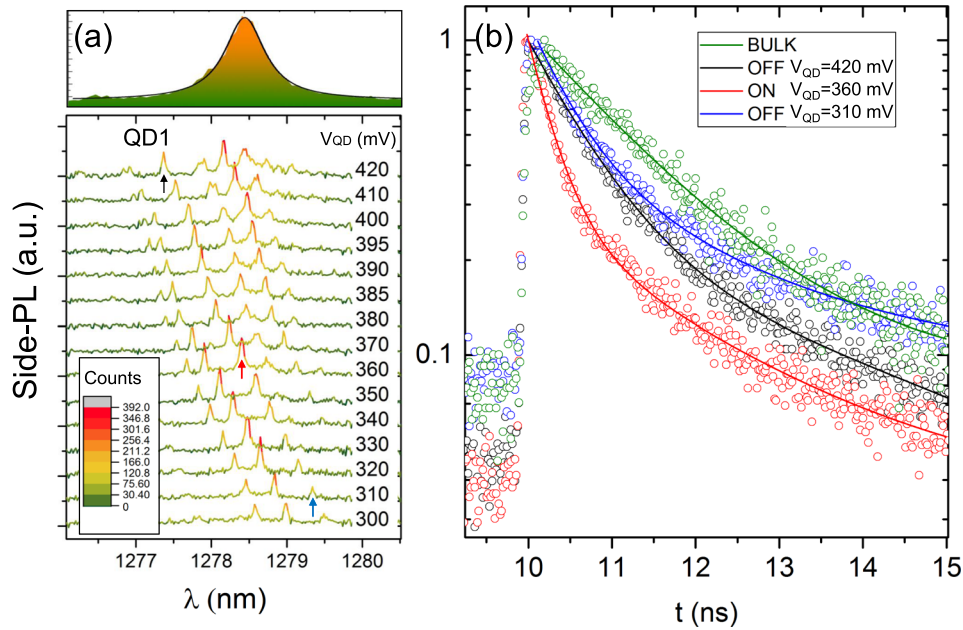


FIG. 4. Electrical control of QD excitons embedded in a waveguide-coupled cavity mode. [(a), bottom panel] Side-PL signal acquired while sweeping the QD-voltage at low pumping power $P = 10 \mu\text{W}$ with an integration time of 30 s. [(a), top panel] High-power side-PL intensity of the cavity mode, $P = 0.7 \text{ mW}$. (b) Decay curves of QD1 positioned at several detunings with respect to the cavity mode: (red dots) on resonance, (black dots) blue-shifted, (blue dots) red-shifted, and (green dots) bulk decay traces collected from an ensemble of QDs in a different point of the sample. The continuous lines are obtained from a single (bulk) or double exponential fit.

introduced by the Stark-field, is quantified by the internal quantum efficiency $\eta_i = \frac{\tau_{\text{int}}}{\tau_{\text{int}} + \tau_{\text{phC}}} \approx 0.57$. This relatively low radiative efficiency can be improved by implementing AlGaAs barriers above and below the QD layer to suppress the tunneling rate from the dots.¹⁸

In order to estimate the single-photon rate into the ridge waveguide for applications that foresee the co-integration of tunable sources and detectors on the same circuits,⁴³ we decompose the total coupling efficiency from the source to the external detector in two main contributions: $\eta = \eta_{\text{int}} \cdot \eta_{\text{ext}}$, where $\eta_{\text{int}} = \eta_i \cdot \eta_C \cdot \eta_t \cdot e^{-\alpha L} = 3.8 \times 10^{-2}$ is the chip quantum efficiency from the dot to the cleaved part of the wafer, located $L = 1 \text{ mm}$ away from the photonic crystal region (from the measured η_i , η_C and the simulated η_t values reported above and the α value from Sec. S3 of the [supplementary material](#)), and $\eta_{\text{ext}} = \eta_{\text{facet}} \cdot \eta_{\text{filter}} \cdot \eta_{\text{detector}} = 3.9 \times 10^{-3}$ accounts for (i) the coupling from the RW to the lens fiber $\eta_{\text{facet}} = 3.5 \times 10^{-2}$, (ii) the transmission measured through the bandpass filter $\eta_{\text{filter}} = 0.28$, and (iii) the efficiency of the detector $\eta_{\text{detector}} = 0.4$. Given the total count rate measured on the single-photon detectors $C \approx 5000 \text{ Hz}$, we can estimate the experimental single-photon rate into the RW as $R_{\text{exp}} = \frac{C}{\eta_{\text{ext}}} \approx 1.3 \text{ MHz}$. The difference between this value and the expected single-photon rate at the end of the RW, $R_{\text{th}} = f \times \eta_{\text{int}} = 3.0 \text{ MHz}$, is attributed to the presence of emission channels from charged and multi-excitonic states due to non-resonant excitation.⁴⁴

IV. INTEGRATED HANBURY BROWN-TWISS EXPERIMENT

Routing and splitting single-photon states is one of the basic functionalities required in QPICs. Only few approaches have shown the possibility to build a waveguide circuit featuring integrated quantum emitters. Quantum dots have been directly integrated with heterostructure rib waveguides^{45–47} and with nanobeams surrounded by an air cladding,⁴⁸ in order to carry out an integrated HBT experiment. However, exciting emitters directly embedded in ridge waveguides provides low extraction efficiency due to the low index contrast. On the other hand, the maximum length of suspended nanobeams is limited by the occurrence of bending, buckling, and—in general—mechanical instabilities. These drawbacks can be circumvented by taking the advantages of both approaches using

the hybrid solution presented in the previous paragraphs: the photons can be extracted in a photonic crystal cavity or waveguide region which can provide near-unity beta factors,⁴⁹ while their state can be linearly manipulated by a supported RW circuit.

In this section, we present the design and investigation of a basic linear component, a 50:50 beam splitter based on a multimode interferometer (MMI), compatible with the GaAs double-membrane ridge-waveguide platform. A Hanbury-Brown and Twiss prototype experiment is carried out on the photons generated from emitters integrated in a double-membrane PhC waveguide. The light emitted from this PhC source is split on the same chip and the correlation function is measured using off-chip filters and detectors.

Multimode interference couplers are integrated optical components able to redirect the power injected from N input waveguides into M output waveguides. These devices typically consist of a wide rectangular waveguide that supports a relatively large number of propagating modes. These are excited at the input of the MMI region, propagate with a different phase velocity, and interfere constructively at special locations along the propagation direction.⁵⁰ A splitter can be realized by terminating the waveguide where constructive interference takes place.

Three-dimensional beam propagation methods have been employed to simulate the spatial evolution of the electric field intensity along a 2×2 MMI based on the double-membrane platform. The separation between the inner edges of the access waveguides is set to $0.6 \mu\text{m}$, and the width of the MMI is $6 \mu\text{m}$. Figure 5(a) shows the evolution of the electric field intensity in the MMI region as a function of the propagation distance x , when the fundamental TE eigenmode of the RW is launched into the upper input waveguide ($\lambda = 1.27 \mu\text{m}$). The splitting ratio between the output waveguides can be adjusted by optimizing the length L of the MMI. We found an optimal value $L = 110 \mu\text{m}$, corresponding to a theoretical splitting ratio of 50:50 and an insertion loss of -1.6 dB .

In the following set of experiments, we investigate the operation of this beam splitter at the single-photon level, whereas its classical characterization is reported in the [supplementary material](#). In order to perform an integrated HBT experiment, single-exciton transitions are excited in a PhCWG region connected to one input of the MMI and the generated light is split into two optical channels using the MMI. In this experiment, a QD positioned in the WG part of the c-QED node was chosen, instead of the cavity, due to lower spectral background. Moreover, similar to the

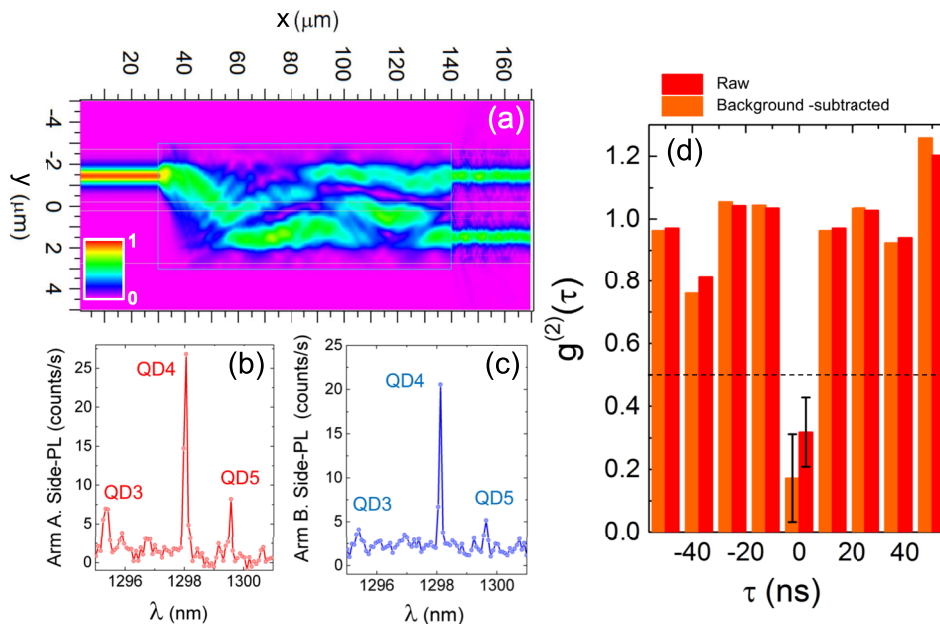


FIG. 5. (a) Calculated intensity of the electric field in a 50:50 beam splitter based on a double-membrane multimode interferometer. [(b) and (c)] Side-PL spectra collected at the two output waveguides of the beam splitter, when the input PhCWG region is excited. (d) Second-order correlation function measured with an excitation power of 300 nW.

single-membrane case, double-membrane PhCWG can in principle provide a near-unity coupling efficiency into a propagating mode. The QD-emission is collected by two distinct fibers positioned at the cleaved facet of the RWs in a butt-coupled configuration and sequentially acquired by using a spectrometer.

Figures 5(b) and 5(c) show the side-PL spectra acquired at the two output arms (labeled A and B) of the beam splitter. Three different QD-lines, named QD3, QD4, and QD5, are visible in both spectra. In particular, the excitonic transition QD4, located at ≈ 1298 nm, shows a splitting ratio of $\approx 56/44$. It is worth mentioning that the count rates in these measurements are comparable with count rates obtained in top-collection experiments from similar dots coupled to PhCCs,¹⁸ which qualitatively indicates the efficient extraction and routing of the dot-emission across the chip.

In the following experiments, the dot line QD4 is isolated from the other lines using off-chip filtering. In particular, two long-pass filters (cut-off wavelength 1050 nm) and two tunable band-pass filters are inserted in the two optical paths of the setup, each connected to a superconducting nanowire single-photon detector (SSPD,⁵¹ see S1 of the [supplementary material](#)). The electrical signals generated by the detectors are acquired by a time-correlated counting module for correlation measurements.

Figure 5(d) shows the raw (red bars) and the background-corrected (orange bars) normalized second-order correlation function acquired when QD4 is excited with a pulsed laser diode (power $P_1 \approx 300$ nW) with a repetition rate of 80 MHz and using an integration window of 4 ns. A suppression of the zero-delay peak is evident compared to the peaks at multiples of the repetition period. This constitutes strong evidence that the non-classical nature of these emitters is preserved along the circuit.

The raw histogram acquired with a temporal resolution of 512 ps and the procedure adopted for the background subtraction are reported in Sec. S7 of the [supplementary material](#).

The value of the raw (background-subtracted) second-order correlation function at zero delay is $g^{(2)}(0) = 0.32 \pm 0.11$ ($\bar{g}^{(2)}(0) = 0.17 \pm 0.14$). For an ideal single-photon source and a balanced beam splitter, this value is zero, corresponding to the complete suppression of photon pair detection. We attribute the discrepancy from the ideal case to the relatively high pumping level in this experiment, resulting in an increased probability of generating multi-photon states.⁵² We observed in fact that repeating the same experiment with a higher excitation power ($P_2 \approx 500$ nW) gives a higher multi-photon probability $g^{(2)}(\tau = 0, P = P_2) = 0.46 \pm 0.07$, see S7 of the [supplementary material](#).

V. MULTIPLE C-QED NODES

As a further application of the GaAs technology presented in previous paragraphs, we investigated the possibility to integrate multiple tunable sources on the same chip. Figure 6 shows a fabricated chip for multi-emitter experiments. This comprises two sources equipped with four different diodes, for the simultaneous control of the energy of the cavity modes and quantum dots of each source.

These two PhC sources are integrated with ridge waveguides, which are then connected to the inputs of a MMI via two S-bends (S_1, S_2) as shown in Fig. 6(a). We adopt the optimized designs of the MMI presented in Sec. IV. The output of the MMI is integrated with two S-bends (S_3, S_4), which redirect the QD-light to the cleaved part of the wafer. The radius of curvature of S_1 and S_2 (S_3 and S_4) is $1191 \mu\text{m}$ ($1740 \mu\text{m}$). In the following experiments, two external lensed fibres are positioned at the end of the two RWs to collect the QD-emission from both facets of the RWs, as described in S1 of the [supplementary material](#). The distance between the PhC nodes ($w = 22 \mu\text{m}$) is designed to excite both PhC nodes with a pair of laser spots focused by the same objective. A set of isolation trenches is deeply etched around the device and in between the two PhC nodes to provide electrical isolation. For the cavity and QD diodes, we employ two series of mesas in the $\{n - p_{QD} - n - p_{CAV} - n\}$ configuration.

A. Bringing two cavity modes into resonance

First, we investigated the possibility to individually control the cavity resonances of two adjacent devices, with the aim of bringing two modes into mutual resonance. Figure 7(a) shows the PL signal

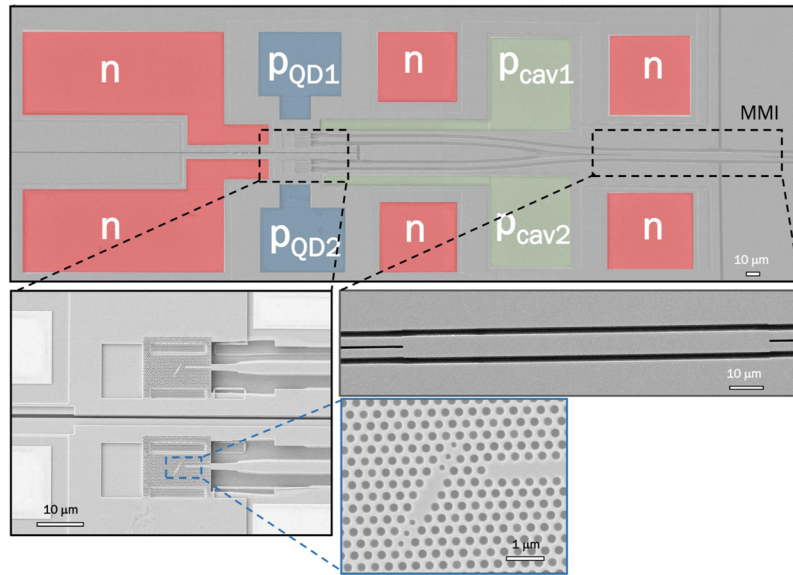


FIG. 6. SEM pictures of the fabricated chip with two integrated single-photon sources. Four sets of diodes are fabricated to tune the cavity and quantum dot energy of the two cavity-emitter systems. Only the top membrane of the architecture is shown.

collected from one output of the beam splitter when the cavity region of one of the two photonic crystal structures (A or B) is excited. These PL spectra are acquired while varying the voltage of node B (V_{CAV}^B) from -1 V to -3 V while the cavity contact of A and the two Stark contacts are left in open circuit.

The power of the 780 nm laser diode is sufficiently high ($P = 500 \mu\text{W}$) that only the emission from the cavity mode is observed. A blueshift of cavity modes is observed for both resonators indicating the presence of a non-negligible cross talk. The sign of the mechanically induced spectral shift shows that the character of these modes is anti-symmetric. The resonant wavelength of cavity B, initially red-shifted with respect to cavity A, crosses the resonance of cavity A at $V_{CAV}^B \approx -2.2$ V.

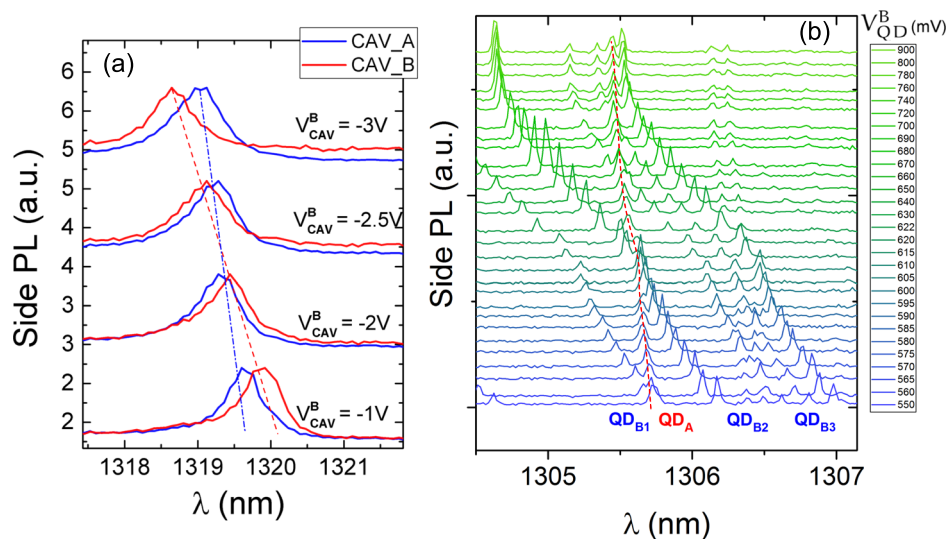


FIG. 7. (a) Electromechanical tuning of a pair of cavities modes into mutual resonance. The dashed lines serve as guides for the eye. (b) Single dot PL collected at one output of the beam splitter by simultaneously exciting two PhCWGs labeled “A” and “B,” and varying the Stark-voltage of node B. Several excitonic lines located in the node B (QD_{B1} , QD_{B2} , and QD_{B3}) are tuned into resonance with an exciton positioned in the node A (QD_A).

It is convenient to define the cavity cross tuning coefficient as $\xi_{CAV} = \frac{\Delta\lambda_{CAV}^A}{\Delta\lambda_{CAV}^B}$. By measuring the cross-tuning over four nominally identical devices, we obtained $\xi_{CAV} = 0.53 \pm 0.11$. We speculate that this cross talk takes place at the MMI, which constitutes the only electrical path interconnecting the two nodes. In the future, the use of a directional coupler or better isolation schemes—such as proton implantation⁵³ or the removal of doped layers in the passive region—might reduce this effect, which in any case does not prevent controlling the spectral alignment of the two cavities compensating their initial spectral misalignment.

B. Bringing two excitons into resonance

Figure 7(b) shows a set of PL spectra collected from one output of the beam splitter, when the regions of two neighboring PhCWGs are simultaneously excited by the 780 nm laser diode set to 1 μ W. We attributed the QD-lines to node A or B, by comparing these spectra with the ones obtained sequentially exciting the two regions. The QD-signal is collected by varying the voltage applied to the QD-diode of node B (V_{QD}^B) from 550 mV to 900 mV (lines from blue to green). When V_{QD}^B is increased, a blue shift of all the QD-lines as a function of the Stark-voltage is observed, as expected by the reduction of the built-in field of the diode in the forward bias.¹⁸ In particular, the excitonic transition QD_A is brought on resonance with several QD-lines generated in the node B (QD_{B1} , QD_{B2} , QD_{B3}). An energy-matching condition is achieved with QD_{B1} at $V_{QD}^B = 550$ mV ($\lambda = 1305.73$ nm), with QD_{B2} at $V_{QD}^B = 600$ mV ($\lambda = 1305.66$ nm), and with a group of spectrally closed lines labeled QD_{B3} for $V_{QD}^B > 650$ mV ($\lambda < 1305.51$ nm). For the voltage values investigated in these experiments, the tuning range of the QD-lines embedded in node B is $\Delta\lambda_{QD}^B = 1.54$ nm, while QD_A shows a cross-tuning of $\Delta\lambda_{QD}^A = 0.29$ nm. The quantum dot cross tuning coefficient can be extracted as $\xi_{QD} = \frac{\Delta\lambda_{QD}^A}{\Delta\lambda_{QD}^B} \approx 0.19$. This relatively small cross talk greatly facilitates the energy-matching of remote QDs, which is one of the key challenges to generate indistinguishable single photons from multiple integrated emitters. We speculate that the difference between the QD and CAV cross-tuning coefficients is related to the different doping concentration and/or thickness variations induced by the fabrication process between the p-doped layers of the cavity and quantum dot diodes. In the experiments reported so far, the use of the above-bandgap excitation schemes represents the main limitation in obtaining Fourier-transformed limited single photons and, consequently, hinders the generation of indistinguishable photons from remote sources. In the future, the coherence time of the QD emission can be improved by making use of resonant or quasi-resonant excitation schemes in order to perform Hong-Ou-Mandel experiments from distinct sources integrated on the same chip.

VI. CONCLUSIONS

In summary, we have presented a photonic platform based on a double-membrane heterostructure which combines electrically tunable single-photon sources with mechanically reconfigurable photonic crystal elements. The spontaneous emission of quantum dots enhanced by tunable cavity modes has been coupled to ridge waveguides able to manipulate the photonic state with low-losses. In addition, we have shown that by modifying the Stark-field across the quantum dot region of these devices, energy-tunable single-exciton lines can be funnelled into this passive architecture. By controlling the cavity-emitter detuning in these c-QED nodes, Purcell-enhanced emission from single excitons into a waveguide has been demonstrated. This platform has been further integrated with a balanced beam splitter. An integrated Hanbury-Brown and Twiss experiment, featuring a source and a splitter on the same chip, has been carried out. Finally, we outlined some avenues to prove the scalability of these sources in a photonic circuit. We have demonstrated the energy control of distinct cavities and emitters located on the same chip. Gaining control over the spatial alignment of cavity-emitter nodes, either via site-controlled growth or via the fabrication of cavities on a pre-characterized self-assembled quantum dot, will be important to achieve a high yield in the cavity coupling. Besides, by exploiting resonant excitation strategies both the coherence properties and the brightness of these single-photon sources can be significantly enhanced.³⁰ Finally, the mechanical reconfigurability developed in this work can be further exploited to build other photonic elements,

such as phase shifters and switches,³⁴ essential to demultiplex a train of single-photons into many spatial channels.⁵⁴

SUPPLEMENTARY MATERIAL

See [supplementary material](#) for the description of the setup employed for the electro-optical characterization of the devices and for further details about the fabrication process and the measurements reported in the main text.

ACKNOWLEDGMENTS

This research was financially supported by the Dutch Technology Foundation STW, Applied Science Division of NWO, the Technology Program of the Ministry of Economic Affairs under Project Nos. 10380 and 12662 and by NanoNextNL, a micro and nanotechnology program of the Dutch Ministry of Economic Affairs, Agriculture and Innovation and 130 partners. This work is also part of the research program of the Foundation for Fundamental Research on Matter (FOM), which is financially supported by the Netherlands organization for Scientific Research (NWO). M.P. acknowledges L. Midolo, S. Fattah Poor, and R. W. van der Heijden for the useful discussions.

- ¹ P. Lodahl, S. Mahmoodian, and S. Stobbe, *Rev. Mod. Phys.* **87**, 347 (2015).
- ² C. P. Dietrich, A. Fiore, M. G. Thompson, M. Kamp, and S. Höfling, *Laser Photonics Rev.* **10**, 857 (2016).
- ³ S. Buckley, K. Rivoire, and J. Vučković, *Rep. Prog. Phys.* **75**, 126503 (2012).
- ⁴ P. Senellart, G. Solomon, and A. White, *Nat. Nanotechnol.* **12**, 1026 (2017).
- ⁵ See <http://Quandela.com> for information about commercially available single-photon sources (2017).
- ⁶ See <http://sparrowquantum.com> for information about commercially available single-photon sources (2017).
- ⁷ A. Faraon and J. Vučković, *Appl. Phys. Lett.* **95**, 043102 (2009).
- ⁸ T. Cai, R. Bose, G. S. Solomon, and E. Waks, *Appl. Phys. Lett.* **102**, 141118 (2013).
- ⁹ A. Y. Piggott, K. G. Lagoudakis, T. Sarmiento, M. Bajcsy, G. Shambat, and J. Vučković, *Opt. Express* **22**, 15017 (2014).
- ¹⁰ F. Raineri, C. Cojocar, R. Raj, P. Monnier, A. Levenson, C. Seassal, X. Letartre, and P. Viktorovitch, *Opt. Lett.* **30**, 64 (2005).
- ¹¹ I. Fushman, E. Waks, D. Englund, N. Stoltz, P. Petroff, and J. Vučković, *Appl. Phys. Lett.* **90**, 091118 (2007).
- ¹² I. W. Frank, P. B. Deotare, M. W. McCutcheon, and M. Lončar, *Opt. Express* **18**, 8705 (2010).
- ¹³ R. Perahia, J. D. Cohen, S. Meenehan, T. P. M. Alegre, and O. Painter, *Appl. Phys. Lett.* **97**, 191112 (2010).
- ¹⁴ L. Midolo, P. van Veldhoven, M. Dunder, R. Notzel, and A. Fiore, *Appl. Phys. Lett.* **98**, 211120 (2011).
- ¹⁵ L. Midolo, A. Schliesser, and A. Fiore, *Nat. Nanotechnol.* **13**, 11 (2018).
- ¹⁶ S. Fattah Poor, T. Hoang, L. Midolo, C. Dietrich, L. Li, E. Linfield, J. Schouwenberg, T. Xia, F. Pagliano, F. Van Otten *et al.*, *Appl. Phys. Lett.* **102**, 131105 (2013).
- ¹⁷ M. Davanco, J. Liu, L. Sapienza, C.-Z. Zhang, J. V. M. Cardoso, V. Verma, R. Mirin, S. W. Nam, L. Liu, and K. Srinivasan, *Nat. Commun.* **8**, 889 (2017).
- ¹⁸ M. Petruzzella, T. Xia, F. Pagliano, S. Birindelli, L. Midolo, Z. Zobenica, L. Li, E. Linfield, and A. Fiore, *Appl. Phys. Lett.* **107**, 141109 (2015).
- ¹⁹ B. Alloing, C. Zinoni, V. Zwiller, L. Li, C. Monat, M. Gobet, G. Buchs, A. Fiore, E. Pelucchi, and E. Kapon, *Appl. Phys. Lett.* **86**, 101908 (2005).
- ²⁰ E. Waks and J. Vuckovic, *Opt. Express* **13**, 5064 (2005).
- ²¹ G.-H. Kim, Y.-H. Lee, A. Shinya, and M. Notomi, *Opt. Express* **12**, 6624 (2004).
- ²² P.-T. Lee, T.-W. Lu, C.-M. Yu, and C.-C. Tseng, *Opt. Express* **15**, 9450 (2007).
- ²³ R. Coles, N. Prtljaga, B. Royall, I. J. Luxmoore, A. Fox, and M. Skolnick, *Opt. Express* **22**, 2376 (2014).
- ²⁴ K. Nozaki, H. Watanabe, and T. Baba, *Appl. Phys. Lett.* **92**, 021108 (2008).
- ²⁵ C. Bentham, I. Itskevich, R. Coles, B. Royall, E. Clarke, J. O'Hara, N. Prtljaga, A. Fox, M. Skolnick, and L. Wilson, *Appl. Phys. Lett.* **106**, 221101 (2015).
- ²⁶ A. Faraon, E. Waks, D. Englund, I. Fushman, and J. Vučković, *Appl. Phys. Lett.* **90**, 073102 (2007).
- ²⁷ T. Malhotra, R.-C. Ge, M. K. Dezfouli, A. Badolato, N. Vamivakas, and S. Hughes, *Opt. Express* **24**, 13574 (2016).
- ²⁸ A. Schwagmann, S. Kalliakos, D. J. Ellis, I. Farrer, J. P. Griffiths, G. A. Jones, D. A. Ritchie, and A. J. Shields, *Opt. Express* **20**, 28614 (2012).
- ²⁹ L. Lu, A. Mock, and J. O'Brien, *J. Opt.* **14**, 055502 (2012).
- ³⁰ F. Liu, A. Brash, J. O'Hara, L. Martins, C. Phillips, R. Coles, B. Royall, E. Clarke, C. Bentham, N. Prtljaga *et al.*, "High Purcell factor generation of indistinguishable on-chip single photons," *Nat. Nanotechnol.* (published online).
- ³¹ Ž. Zobenica, R. W. Heijden, M. Petruzzella, F. Pagliano, R. Leijssen, T. Xia, L. Midolo, M. Cotrufo, Y. Cho, F. W. Otten *et al.*, *Nat. Commun.* **8**, 2216 (2017).
- ³² J. D. Joannopoulos, S. G. Johnson, J. N. Winn, and R. D. Meade, *Photonic Crystals: Molding the Flow of Light* (Princeton University Press, 2011).
- ³³ M. Petruzzella, F. La China, F. Intonti, N. Caselli, M. De Pas, F. van Otten, M. Gurioli, and A. Fiore, *Phys. Rev. B* **94**, 115413 (2016).

- ³⁴ M. Petruzzella, Ž. Zobenica, M. Cotrufo, V. Zardetto, A. Mameli, F. Pagliano, S. Koelling, F. van Otten, F. Roozeboom, W. Kessels *et al.*, *Opt. Express* **26**, 3882 (2018).
- ³⁵ S. G. Johnson, P. Bienstman, M. Skorobogatiy, M. Ibanescu, E. Lidorikis, and J. Joannopoulos, *Phys. Rev. E* **66**, 066608 (2002).
- ³⁶ E. Iwase, P.-C. Hui, D. Woolf, A. W. Rodriguez, S. G. Johnson, F. Capasso, and M. Lončar, *J. Micromech. Microeng.* **22**, 065028 (2012).
- ³⁷ D. P. Kelly, M. W. Pruessner, K. Amarnath, M. Datta, S. Kanakaraju, L. C. Calhoun, and R. Ghodssi, *IEEE Photonics Technol. Lett.* **16**, 1298 (2004).
- ³⁸ T. Stievater, W. Rabinovich, D. Park, J. Khurgin, S. Kanakaraju, and C. Richardson, *Opt. Express* **16**, 2621 (2008).
- ³⁹ C. Zinoni, B. Alloing, C. Monat, V. Zwiller, L. Li, A. Fiore, L. Lunghi, A. Gerardino, H. De Riedmatten, H. Zbinden *et al.*, *Appl. Phys. Lett.* **88**, 131102 (2006).
- ⁴⁰ T. B. Hoang, J. Beetz, M. Lerner, L. Midolo, M. Kamp, S. Höfling, and A. Fiore, *Opt. Express* **20**, 21758 (2012).
- ⁴¹ M. Petruzzella, F. Pagliano, Ž. Zobenica, S. Birindelli, M. Cotrufo, F. van Otten, R. van der Heijden, and A. Fiore, *Appl. Phys. Lett.* **111**, 251101 (2017).
- ⁴² D. Englund, D. Fattal, E. Waks, G. Solomon, B. Zhang, T. Nakaoka, Y. Arakawa, Y. Yamamoto, and J. Vučković, *Phys. Rev. Lett.* **95**, 013904 (2005).
- ⁴³ G. E. Digeronimo, M. Petruzzella, S. Birindelli, R. Gaudio, S. Fattah Poor, F. W. van Otten, and A. Fiore, *Photonics* (Multidisciplinary Digital Publishing Institute, 2016), Vol. 3, p. 55.
- ⁴⁴ N. Chauvin, C. Zinoni, M. Francardi, A. Gerardino, L. Balet, B. Alloing, L. Li, and A. Fiore, *Phys. Rev. B* **80**, 241306 (2009).
- ⁴⁵ K. D. Jöns, U. Rengstl, M. Oster, F. Hargart, M. Heldmaier, S. Bounouar, S. M. Ulrich, M. Jetter, and P. Michler, *J. Phys. D: Appl. Phys.* **48**, 085101 (2015).
- ⁴⁶ P. Stepanov, A. Delga, X. Zang, J. Bleuse, E. Dupuy, E. Peinke, P. Lalanne, J.-M. Gérard, and J. Claudon, *Appl. Phys. Lett.* **106**, 041112 (2015).
- ⁴⁷ M. Schwartz, U. Rengstl, T. Herzog, M. Paul, J. Kettler, S. L. Portalupi, M. Jetter, and P. Michler, *Opt. Express* **24**, 3089 (2016).
- ⁴⁸ N. Prtljaga, R. Coles, J. O'Hara, B. Royall, E. Clarke, A. Fox, and M. Skolnick, *Appl. Phys. Lett.* **104**, 231107 (2014).
- ⁴⁹ M. Arcari, I. Söllner, A. Javadi, S. L. Hansen, S. Mahmoodian, J. Liu, H. Thyrestrup, E. H. Lee, J. D. Song, S. Stobbe *et al.*, *Phys. Rev. Lett.* **113**, 093603 (2014).
- ⁵⁰ L. B. Soldano and E. C. Pennings, *J. Lightwave Technol.* **13**, 615 (1995).
- ⁵¹ See <http://www.scontel.ru> for information about the employed single-photon detectors.
- ⁵² A. Shields, R. Stevenson, R. Thompson, Z. Yuan, and B. Kardynal, *Generation of Single Photons Using Semiconductor Quantum Dots* (Elsevier, 2002).
- ⁵³ A. Szerling, K. Kosiel, M. Kozubal, M. Myśliwiec, R. Jakiela, M. Kuc, T. Czyszanowski, R. Kruszka, K. Pagowska, P. Karbownik *et al.*, *Semicond. Sci. Technol.* **31**, 075010 (2016).
- ⁵⁴ L. Midolo, S. L. Hansen, W. Zhang, C. Papon, R. Schott, A. Ludwig, A. D. Wieck, P. Lodahl, and S. Stobbe, *Opt. Express* **25**, 33514 (2017).